Normalized energy-norm imaging condition for elastic reverse time migration

Can Oren & Jeffrey Shragge
Center for Wave Phenomena and Dept. of Geophysics, Colorado School of Mines, Golden CO 80401
coren@mines.edu

ABSTRACT
Elastic wavefield imaging of multicomponent seismic data can provide additional complementary information about subsurface geological structures (e.g., elastic properties and fracture distribution) relative to single-component acoustic imaging. We propose a novel imaging condition for elastic reverse time migration using deconvolution energy normalization. Being derived from the existing energy-norm imaging operator, the proposed approach uses multicomponent seismic data without wave-mode decomposition, outputs a scalar image with attenuated backscattering artifacts, and does not suffer from polarity reversal at normal incidence. Realistic synthetic and field data experiments show the effectiveness of the normalized energy-norm imaging condition in balancing the image amplitudes as well as enhancing the vertical spatial resolution in comparison with its energy-norm counterpart.

Key words: elastic imaging, multicomponent, imaging condition, conservation of energy, DAS VSP, OBN, OBC

1 INTRODUCTION

Wavefield-based seismic migration is an effective approach for constructing images of complex subsurface structure. Compared to the conventional acoustic migration using single-component seismic data, elastic migration with multicomponent data can provide more detailed subsurface information such as fracture distributions and elastic properties. Elastic reverse time migration (ERTM) is commonly known to be a robust wavefield imaging tool that maps multicomponent seismic data to a subsurface image using the following steps: (1) forward model a source wavefield using an estimated wavelet while saving this wavefield at the domain boundaries, (2) reconstruct the source and receiver wavefields through reverse-time propagation, and (3) evaluate an imaging condition on-the-fly to extract an image of the earth's reflectivity from the extrapolated source and receiver wavefields (Chang and McMechan, 1987; Yan and Sava, 2008; Yan and Xie, 2012).

In recent years, numerous imaging conditions have been proposed for elastic wavefield migration of multicomponent seismic data (Etgen, 1988; Sun et al., 2006; Yan and Sava, 2008; Rocha et al., 2016). For elastic media, a common practice involves decomposing the wavefield into its P- and S-wave mode components prior to imaging condition evaluation (Dellinger and Etgen, 1990). The wave-mode separation step is typically followed by zero-lag crosscorrelation of specific wave modes from source and receiver wavefields leading to multiple subsurface images for a given experiment. In such cases, polarity reversal occurs due to changes in the elastic wavefield polarization, which deteriorates the image quality after non-constructive stacking over experiments (Balch and Erdemir, 1994).

To mitigate the polarity reversal issue, several corrections can be implemented either in the imaging condition (Duan and Sava, 2015; Yang et al., 2021) or before/after imaging in shot/angle domain (Rosales et al., 2008; Du et al., 2012). Furthermore, if the migration earth model contains sharp contrasts, low-wavenumber backscattering artifacts contaminate the imaging results, thus degrading the image quality (Yan and Xie, 2012). To alleviate all the aforementioned obstacles in elastic imaging, Rocha et al. (2016) propose the energy-norm imaging condition based on the energy conservation principle and elastic wavefields. This approach produces a scalar energy image that provides a concise representation of the imaged structures, thus facilitating geological interpretation.

In this study, we first review the equations of elastodynamics and present the energy-norm imaging condition on which our deconvolution energy normalization imaging formalism is based. Next, we present two 2D synthetic and one 2D field data imaging examples using distributed acoustic sensing (DAS) vertical seismic profiling (VSP) and ocean-bottom node (OBN) and cable (OBC) data sets that demonstrate the efficacy of the proposed approach compared to its energy-norm counterpart for constructing subsurface images. Finally, we highlight the advantages offered by the normalized energy-norm imaging approach.

2 THEORY

Assuming linear elasticity, we consider the anisotropic elastic wave equation with no external sources (Aki and Richards, 2002):

$$\rho\,\ddot{\mathbf{u}} = \nabla\cdot\left[\,\underline{\underline{\boldsymbol{c}}}\,\nabla\mathbf{u}\,\right], \tag{1}$$

where $\mathbf{u} = \mathbf{u}(\mathbf{x}, t, e)$ is the displacement field as a function of space $\mathbf{x}$, time t, and the experiment index e, $\rho = \rho(\mathbf{x})$ is the medium density, $\underline{\underline{\boldsymbol{c}}} = \underline{\underline{\boldsymbol{c}}}(\mathbf{x})$ is the stiffness tensor, and the underlying double bar indicates that the stiffness is a fourth-rank tensor. The two superscript dots on $\ddot{\mathbf{u}}$ indicate second-order time differentiation, and ∇ and $\nabla\cdot$ are the gradient and divergence operators, respectively. Given the spatial distribution of the stiffness tensor $\underline{\underline{\boldsymbol{c}}}$, a displacement field $\mathbf{u}$ computed via numerical implementation of equation 1 can be extrapolated forward and backward in time between the window start and end times, $t = [0, T]$ s.

Equation 1 can be derived from two key relationships: (1) a linear constitutive relation (Hooke's law) describing the elastic material properties through the stiffness tensor $\underline{\underline{\boldsymbol{c}}}$

$$\underline{\boldsymbol{\sigma}} = \underline{\underline{\boldsymbol{c}}}\;\underline{\boldsymbol{\varepsilon}}, \tag{2}$$

which relates the strain tensor $\underline{\boldsymbol{\varepsilon}} = \underline{\boldsymbol{\varepsilon}}(\mathbf{x}, t, e)$ to the Cauchy stress tensor $\underline{\boldsymbol{\sigma}} = \underline{\boldsymbol{\sigma}}(\mathbf{x}, t, e)$; and (2) infinitesimal displacements ($\|\underline{\boldsymbol{\varepsilon}}\| \ll 1$), which leads to a linear relationship between $\underline{\boldsymbol{\varepsilon}}$, $\mathbf{u}$, and its transpose $\mathbf{u}^{\mathrm{T}}$

$$\underline{\boldsymbol{\varepsilon}} = \frac{1}{2}\big(\nabla\mathbf{u} + \nabla\mathbf{u}^{\mathrm{T}}\big). \tag{3}$$

The wavefield particle velocities, stresses, and strains allow one to formulate a number of (anisotropic) elastic imaging conditions. Rocha et al. (2017) use these wavefield variables to specify an anisotropic elastic energy imaging condition and demonstrate its use in ERTM to generate an interpretable scalar image:

$$I_E = \sum_{e,t}\left(\rho\,\dot{\mathbf{u}}_S\cdot\dot{\mathbf{u}}_R^{\dagger} - (\underline{\underline{\boldsymbol{c}}}\nabla\mathbf{u}_S) : \nabla\mathbf{u}_R^{\dagger}\right), \tag{4}$$

where $\dot{\mathbf{u}}_S$ and $\dot{\mathbf{u}}_R^{\dagger}$ respectively denote the source and receiver particle velocity vectors; $|\cdot|$ represents vector norm; and symbols † and : indicate wavefield adjoint and the Frobenius product between two tensors, respectively. Equation 4 corresponds to the Lagrangian operator defined as the difference between the wavefield kinetic and potential energy terms (Ben-Menahem and Singh, 1981) that measures the differential wavefield energy that attenuates the low-wavenumber artifacts (Rocha et al., 2017). The other advantages of this approach are that it neither requires elastic wavefield decomposition nor suffers from polarity reversal issues.

We reformulate the potential term of the energy imaging condition (equation 4) to produce a scalar normalized energy ERTM image:

$$I_{EN} = \sum_{e,t}\frac{\left(\rho\,\dot{\mathbf{u}}_S\cdot\dot{\mathbf{u}}_R^{\dagger} - \underline{\boldsymbol{\sigma}}_S : \underline{\boldsymbol{\varepsilon}}_R^{\dagger}\right)}{\sqrt{\left(\rho\,|\dot{\mathbf{u}}_S|^2 + \underline{\boldsymbol{\sigma}}_S : \underline{\boldsymbol{\varepsilon}}_S\right)\left(\rho\,|\dot{\mathbf{u}}_R^{\dagger}|^2 + \underline{\boldsymbol{\sigma}}_R^{\dagger} : \underline{\boldsymbol{\varepsilon}}_R^{\dagger}\right)} + \epsilon^2}, \tag{5}$$

where the Lagrangian operator in the nominator is now formed by using the source particle velocity and stress fields $[\dot{\mathbf{u}}_S, \underline{\boldsymbol{\sigma}}_S]$ along with the receiver (adjoint) particle velocity and strain fields $[\dot{\mathbf{u}}_R^{\dagger}, \underline{\boldsymbol{\varepsilon}}_R^{\dagger}]$. The two squared terms in the denominator are the total source and receiver wavefield energy that corresponds to the Hamiltonian operator (Ben-Menahem and Singh, 1981) and ϵ^2 is a small, positive quantity used to stabilize the division. This normalization operation plays a deconvolution role, which tends to improve the vertical spatial resolution and generate more balanced image amplitudes. Moreover, the proposed imaging approach in equation 5 inherits all the aforementioned advantages of the energy-norm imaging condition in equation 4. Note that care must be taken when choosing an ϵ value as this parameter may cause imaging artifacts if too small of a value is selected.

To partially account for irregular illumination, the deconvolution imaging condition is commonly used in acoustic RTM engines where only the source-side wavefield energy is taken into account during normalization (Leveille et al., 2011). However, the proposed imaging operator provides a more natural approach by normalizing the ratio of energy partitioned at an interface by total

wavefield energy available at the interface to generate a dimensionless image. Applying a least-squares ERTM framework (Feng and Schuster, 2017), though, is likely necessary to recover reasonable reflectivity estimates.

3 NUMERICAL EXPERIMENTS

3.1 Experiment 1: Land DAS VSP data

Our first synthetic numerical experiment is based on a DAS VSP acquisition in an onshore borehole environment. We use a modified version of the Barrett unconventional model (Regone et al., 2017) that represents an isotropic elastic (i.e., $[V_P, V_S, \rho]$) land seismic scenario. The DAS VSP survey includes a total of 100 source points with a 40 m shot interval as well as a total of 994 effective receiver locations with an approximate 1.0 m sample spacing. The top and bottom receiver measured depths are 0.076 km and 1.069 km, respectively. Using an Ormsby wavelet specified by corner frequencies $[f_1, f_2, f_3, f_4] = [2, 5, 60, 80]$ Hz, we forward model elastic seismic data with a total record length of 4.0 s and a 0.5 ms sampling rate. We then apply an $f - k$ filter to the DAS recordings to isolate the upgoing wavefields (i.e., P- and S-wave reflections) required for subsurface imaging.

Figure 1 displays the V_P and V_S models together with the source and receiver geometry used in the DAS VSP imaging experiment. Although not shown here, the V_S and ρ models share similar characteristics to the V_P model. To avoid the imaging artifacts caused by receiver wavefield injection along the DAS cable, we sort the shot gathers into common-receiver gathers, which are then directly migrated during the ERTM procedure. This configuration enables us to generate a reciprocal source and receiver geometry (i.e., the sources and receivers are positioned at the borehole and surface, respectively). For the imaging process, we select 96 reciprocal shots along the borehole between 0.1 km and 1.0 km in depth spaced at a 10 m interval. Also note that we use only the displacement field recorded at the vertical component for imaging to mimic a field scenario where the wavefield is typically measured in the borehole fiber-axis direction. However, one should formally extract the along-fiber strain rate and approximately convert it into displacement using, e.g., the approach of Lindsey et al. (2020).

Figure 2a and 2b shows the energy-norm (equation 4) and normalized energy-norm (equation 5) imaging results, respectively. Both images exhibit the horizontal reflectors and the fault structure; however, applying the normalized energy-norm imaging helps to balance the spectral content of the imaged reflectors and reduce the imaging artifacts. Moreover, as shown in Figure 2b, the total wavefield normalization tends to compensate for the limited illumination due to the relatively narrow aperture angle between reciprocal sources and receivers. Although both imaging methods combine all wave modes (i.e., P- and S-wave energy) into a single scalar image, we present the P-wave reflectivity (Figure 2c) for comparison purposes.

3.2 Experiment 2: WAMo OBN data

We next illustrate our elastic imaging framework using a realistic synthetic model generated as part of the Western Australia Modeling (WAMo) project (Shragge et al., 2019a,b). The resulting 3D large-scale geomodel represents a part of the Northern Carnarvon Basin located on Western Australia's North West Shelf. We extract a crossline for each isotropic elastic model parameter $[V_P, V_S, \rho]$ from the original 3D model and design an acquisition geometry consisting of 385 pressure sources with 100 m spacing deployed along the sea surface (red dots) as well as a sparse set of 120 multicomponent OBN stations with 250 m spacing (white dots) (see Figure 3a). We forward model synthetic elastic data using an Ormsby wavelet with a 25 Hz maximum frequency. Similar to the previous numerical experiment, we migrate the common-receiver data due to the sparser node interval.

Figure 3c depicts the normalized energy-norm imaging result for the WAMo model, in which the main reflectors are accurately imaged with more balanced amplitudes particularly below 3.0 km depth due to the normalization in equation 5 relative to the energy-norm image in Figure 3b.

3.3 Experiment 3: Volve North Sea OBC data

We also apply our imaging approach to a 2D subset of a 3D OBC data set from the Volve field, located in the Norwegian North Sea with a 90 m average water depth. One of the main imaging goals is to delineate the complex subchalk reservoir below the base Cretaceous unconformity (Szydlik et al., 2007). We are provided with separated PP and PS shot gathers extracted from a 2D receiver line of 483 shots and 240 receivers with a shot and receiver interval of 25 m. The elastic VTI Volve model is characterized by Thomsen (1986) anisotropy parameters $[V_{P0}, V_{S0}, \epsilon, \delta]$, which are shown in Figure 4. Because the imaging techniques presented herein require displacement data, we treat the PP and PS data subsets as the vertical and horizontal displacement components, respectively. However, we only use the vertical component in the imaging step. Prior to imaging, we low-pass the data at 25 Hz and apply a time gain to compensate for 3D propagation effects.

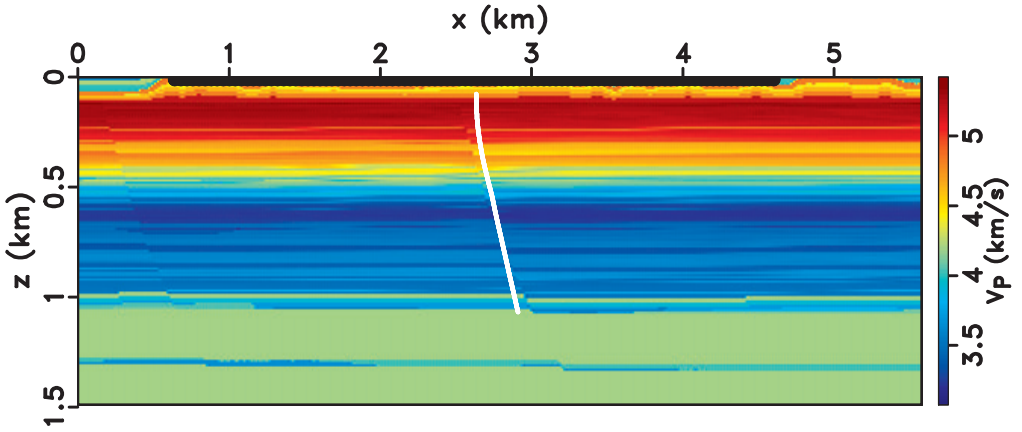

(a)

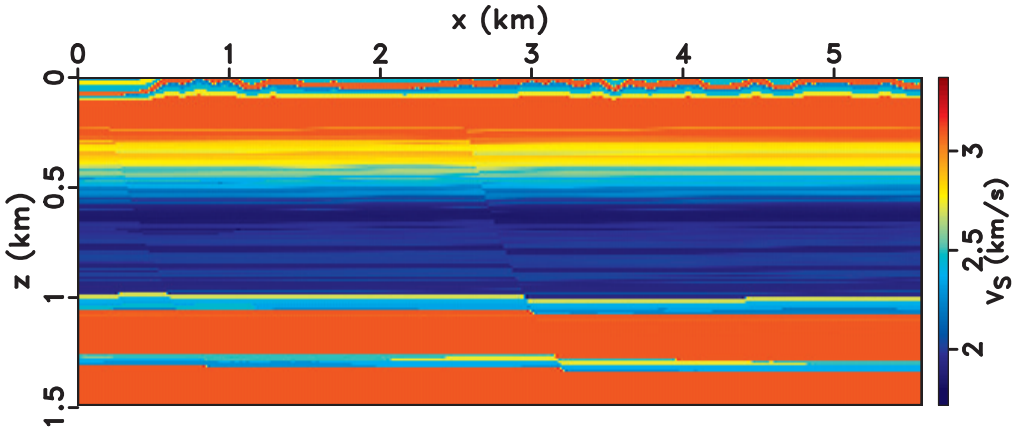

(b)

Figure 1. (a) P- and (b) S-wave velocity models used in the DAS VSP experiment. While the black dots depict the surface source locations, the white dots denote the DAS cable deployed along a deviated well in (a).

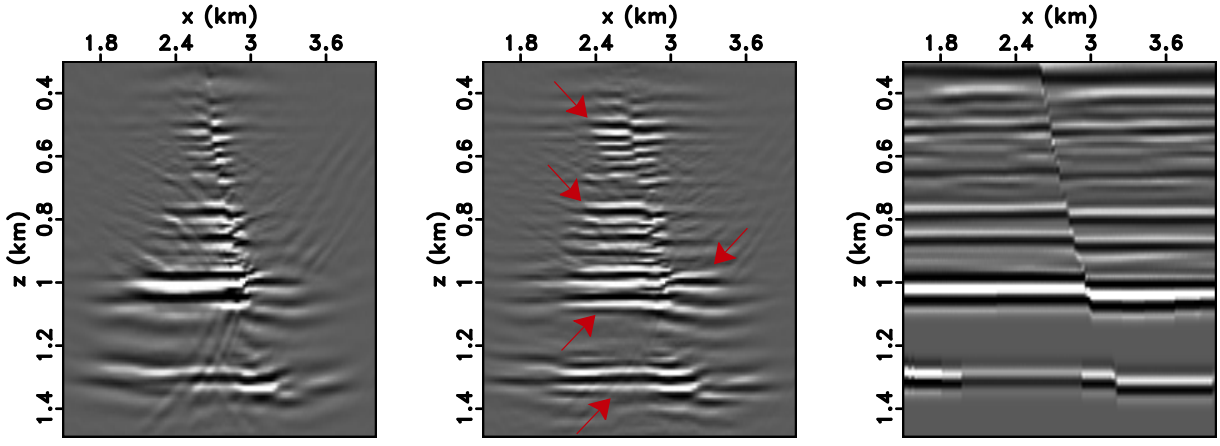

(a) (b) (c)

Figure 2. Zoomed (a) energy-norm and (b) normalized energy-norm ERTM imaging results. (c) The P-wave reflectivity of the Barrett Unconventional model in Figure 1. Red arrows highlight the improved vertical resolution and illumination as well as reduced imaging artifacts in (b) due to the energy normalization relative to the image in (a).

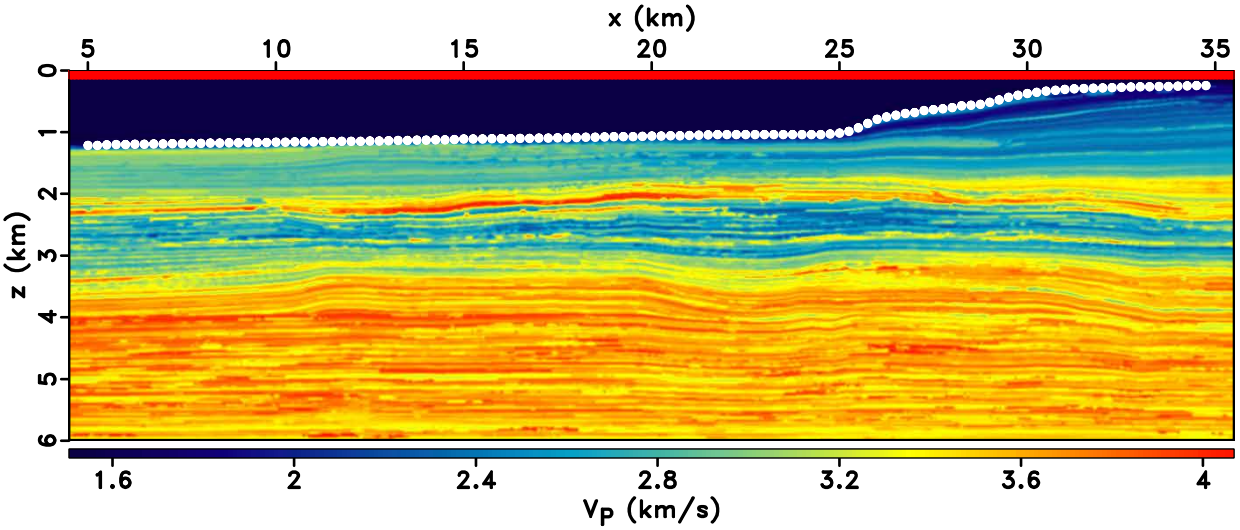

(a)

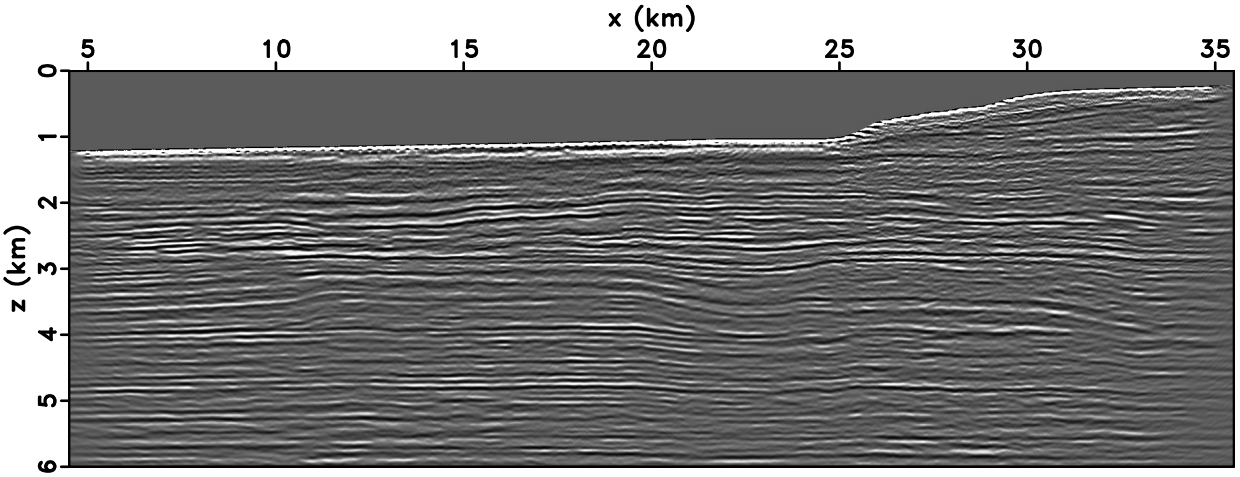

(b)

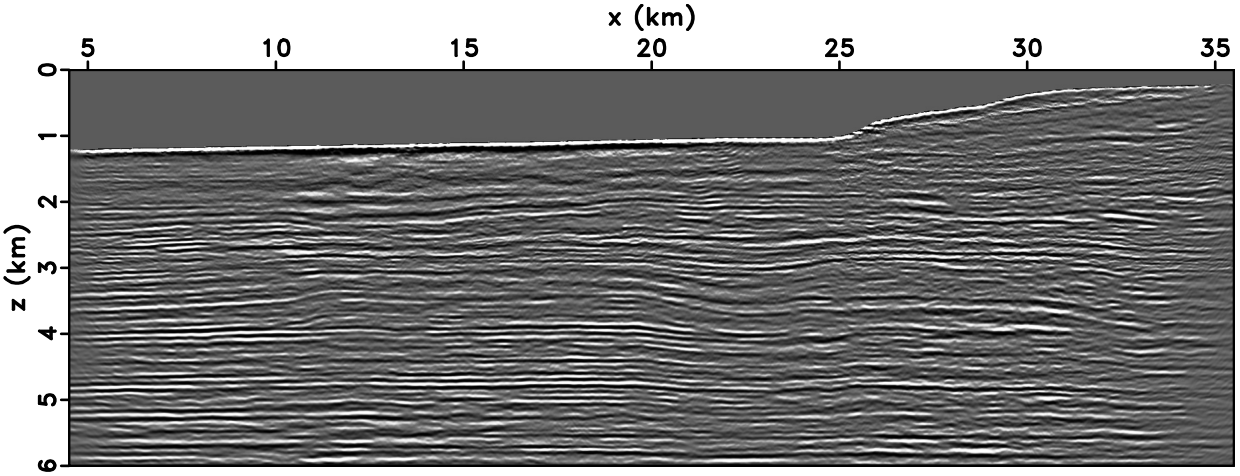

(c)

Figure 3. (a) WAMo V_P model along with the source (red dots) and receiver (white dots) acquisition geometry. Note that the original V_P model ranges between $0 - 40$ km in the lateral direction while the sources are positioned between $0.75 - 39.15$ km. (b) Energy-norm and (c) normalized energy-norm imaging results. Note the more balanced reflector amplitudes and reduction in near-surface artifacts in (c) compared to (b).

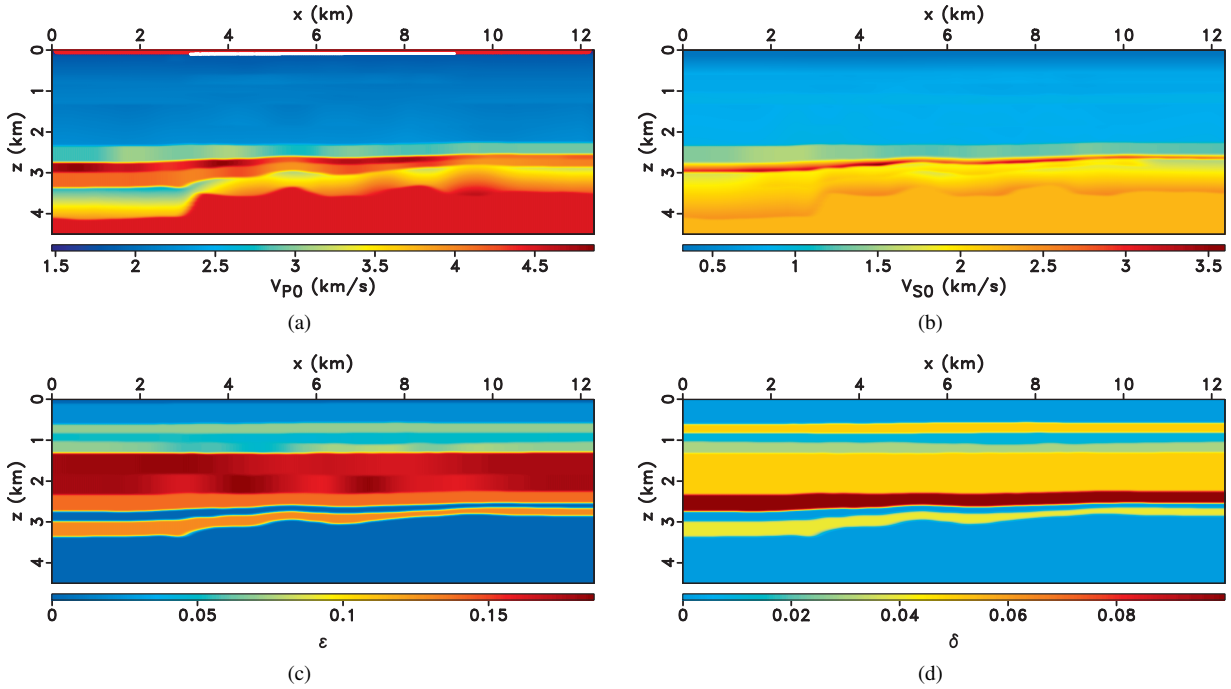

Figure 4. Migration model parameters used for the Volve OBC experiment. (a) P- and (b) S-wave velocities along the vertical symmetry axis; Thomsen parameters (c) ε and (d) δ. The red and white dots in (a) respectively denote 483 pressure sources and 240 multicomponent OBC receivers. The average top water layer is 90 m.

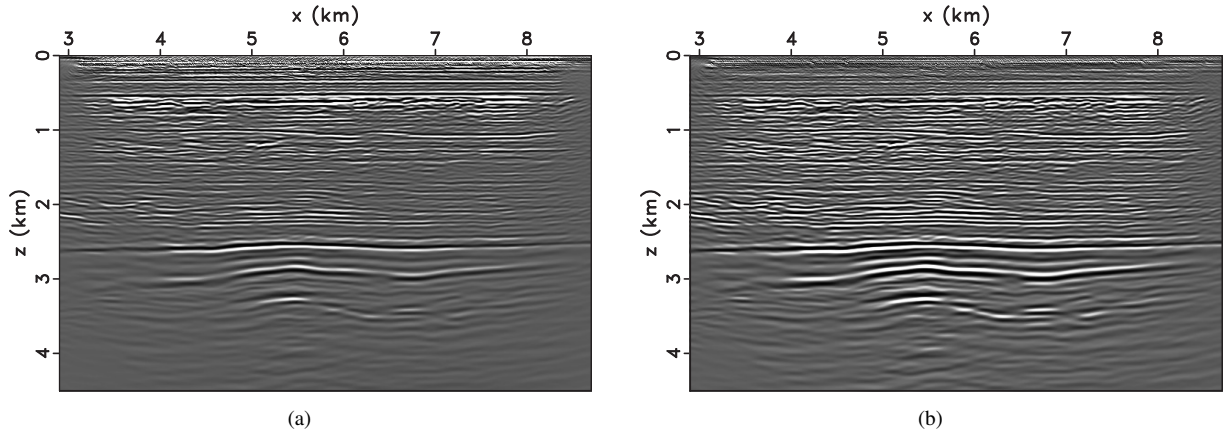

Figure 5. (a) Energy-norm and (b) normalized energy-norm imaging results from the Volve OBC experiment. Note the more balanced reflector amplitudes and reduction in near-surface artifacts in (b) compared to (a).

Compared with the energy-norm image (Figure 5a), the overall reflector amplitudes appear to be more balanced and prominent particularly for the target chalk layer below $z = 2.5$ km in the normalized energy-norm image (Figure 5b). Furthermore, the normalization procedure tends to attenuate most of the imaging artifacts in the shallow sediments located within the zone 0.5 km below mudline. Finally, the imaged reflector at $z = 0.5$ km in Figure 5b exhibits reduced side lobes, thus showing somewhat increased vertical resolution relative to the reflectors observed in Figure 5a.

4 CONCLUSIONS

We present an ERTM-based normalized energy-norm imaging condition that exploits a deconvolution energy normalization and delivers structural images with relatively more balanced amplitudes, higher wavenumbers, and fewer imaging artifacts, all of which facilitate structural interpretation. Because the proposed imaging approach inherits all the advantages of the energy-norm imaging condition, it neither suffers from polarity reversal issues nor requires wave-mode decomposition, and produces scalar images with attenuated backscattering artifacts. We demonstrate the efficacy of the normalized energy imaging operator by using synthetic DAS VSP and OBN as well as field OBC data examples.

5 ACKNOWLEDGEMENTS

We thank the CWP consortium sponsors for their financial support, and acknowledge the sponsors of the WAMo project that lead to the creating of the WAMo model. We are grateful to Statoil ASA and the Volve license partners ExxonMobil E&P Norway AS and Bayerngas Norge AS, for the release of the Volve data set. The views expressed in this paper are the views of the authors and do not necessarily reflect the views of Statoil ASA and the Volve field license partners. The reproducible numerical examples in this paper were generated using the Madagascar software package using the Wendian HPC systems made available through the Colorado School of Mines.

REFERENCES

Aki, K., and P. G. Richards, 2002, Quantitative seismology, 2nd ed.: University Science Books.

Balch, A., and C. Erdemir, 1994, Sign-change correction for prestack migration of P-S converted wave reflections: Geophysical Prospecting, **42**, 637–663.

Ben-Menahem, A., and S. J. Singh, 1981, Seismic waves and sources: Springer-Verlag.

Chang, W.-F., and G. A. McMechan, 1987, Elastic reverse-time migration: Geophysics, **52**, 1365–1375.

Dellinger, J., and J. Etgen, 1990, Wave-field separation in two-dimensional anisotropic media: Geophysics, **55**, 914–919.

Du, Q., Y. Zhu, and J. Ba, 2012, Polarity reversal correction for elastic reverse time migration: Geophysics, **77**, no. 2, S31–S41.

Duan, Y., and P. Sava, 2015, Scalar imaging condition for elastic reverse time migration: Geophysics, **80**, no. 4, S127–S136.

Etgen, J. T., 1988, Prestacked migration of P and SV-waves: 58th Annual International Meeting, SEG, Expanded Abstracts, 972–975.

Feng, Z., and G. T. Schuster, 2017, Elastic least-squares reverse time migration: Geophysics, **82**, no. 2, S143–S157.

Leveille, J. P., I. F. Jones, Z.-Z. Zhou, B. Wang, and F. Liu, 2011, Subsalt imaging for exploration, production, and development: A review: Geophysics, **76**, no. 5, WB3–WB20.

Lindsey, N. J., H. Rademacher, and J. B. Ajo-Franklin, 2020, On the broadband instrument response of fiber-optic DAS arrays: Journal of Geophysical Research: Solid Earth, **125**, e2019JB018145.

Regone, C., J. Stefani, P. Wang, C. Gerea, G. Gonzalez, and M. Oristaglio, 2017, Geologic model building in SEAM Phase II-Land seismic challenges: Leading Edge, **36**, 738–749.

Rocha, D., N. Tanushev, and P. Sava, 2016, Isotropic elastic wavefield imaging using the energy norm: Geophysics, **81**, no. 4, S207–S219.

———, 2017, Anisotropic elastic wavefield imaging using the energy norm: Geophysics, **82**, no. 3, S225–S234.

Rosales, D. A., S. Fomel, B. L. Biondi, and P. C. Sava, 2008, Wave-equation angle-domain common-image gathers for converted waves: Geophysics, **73**, no. 1, S17–S26.

Shragge, J., J. Bourget, D. Lumley, J. Giraud, T. Wilson, A. Iqbal, M. Emami Niri, B. Whitney, T. Potter, T. Miyoshi, and B. Witten, 2019a, The Western Australia Modeling project — Part 1: Geomodel building: Interpretation, **7**, no 4., T773–T791.

Shragge, J., D. Lumley, J. Bourget, T. Potter, T. Miyoshi, B. Witten, J. Giraud, T. Wilson, A. Iqbal, M. Emami Niri, and B. Whitney, 2019b, The Western Australia Modeling project — Part 2: Seismic validation: Interpretation, **7**, no. 4, T793–T807.

Sun, R., G. A. McMechan, C.-S. Lee, J. Chow, and C.-H. Chen, 2006, Prestack scalar reverse-time depth migration of 3D elastic seismic data: Geophysics, **71**, no. 5, S199–S207.

Szydlik, T., P. Smith, S. Way, L. Aamodt, and C. Friedrich, 2007, 3D PP/PS prestack depth migration on the Volve field: First Break, **25**, 43–47.

Thomsen, L., 1986, Weak elastic anisotropy: Geophysics, **51**, 1954–1966.

Yan, J., and P. Sava, 2008, Isotropic angle-domain elastic reverse-time migration: Geophysics, **73**, no. 6, S229–S239.

Yan, R., and X.-B. Xie, 2012, An angle-domain imaging condition for elastic reverse time migration and its application to angle gather extraction: Geophysics, **77**, no. 5, S105–S115.

Yang, K., X. Dong, and J. Zhang, 2021, Polarity-reversal correction for vector-based elastic reverse time migration: Geophysics, **86**, no. 1, S45–S58.